Microcircuits of Functionally Identified Neurons in the Rat Medial Entorhinal Cortex

Andrea Burgalossi, Lucas Herfst, Moritz von Heimendahl, Henning Förste, Kurt Haskic, Martin Schmidt, and Michael Brecht

INVENTORY LIST OF SUPPLEMENTAL FIGURES

	Title	Related to
Figure S1	Recording durations, wake-up from anesthesia and representative spike waveforms	Figure 1
Figure S2	Cytochrome oxidase staining reveals layer 2 patches in parasaggital sections of medial entorhinal cortex	Figure 2
Figure S3	Small layer 2 cytochrome oxidase patches increase in size from dorsal to ventral medial entorhinal cortex	Figure 2
Figure S4	Dendritic morphologies of layer 2 stellate neurons relative to the patchy layer architecture	Figure 2
Figure S5	Lap-by-lap spatial firing analysis of superficial layer neurons	Figure 3
Figure S6	Stability of head-direction firing in large patch cells	Figures 5-6-7
Figure S7	Theta modulation and theta-phase preferences of layer 2, layer 3 and large patch cells of medial entorhinal cortex	Figure 7
Figure S8	Myelin stained tangential sections through the dorsomedial region of medial entorhinal cortex	Figure 8

SUPPLEMENTAL FIGURES

A Layer 2

5 cm/s

20 s

Antidote
t ~ -3 min

Start
t=0

B

Number of Recordings

□ Deliberately Terminated
Recordings

0   400   800   1200
Recording Time (s)

C

Number of Recordings

0   400   800   1200   1600   2000
Distance Travelled (cm)
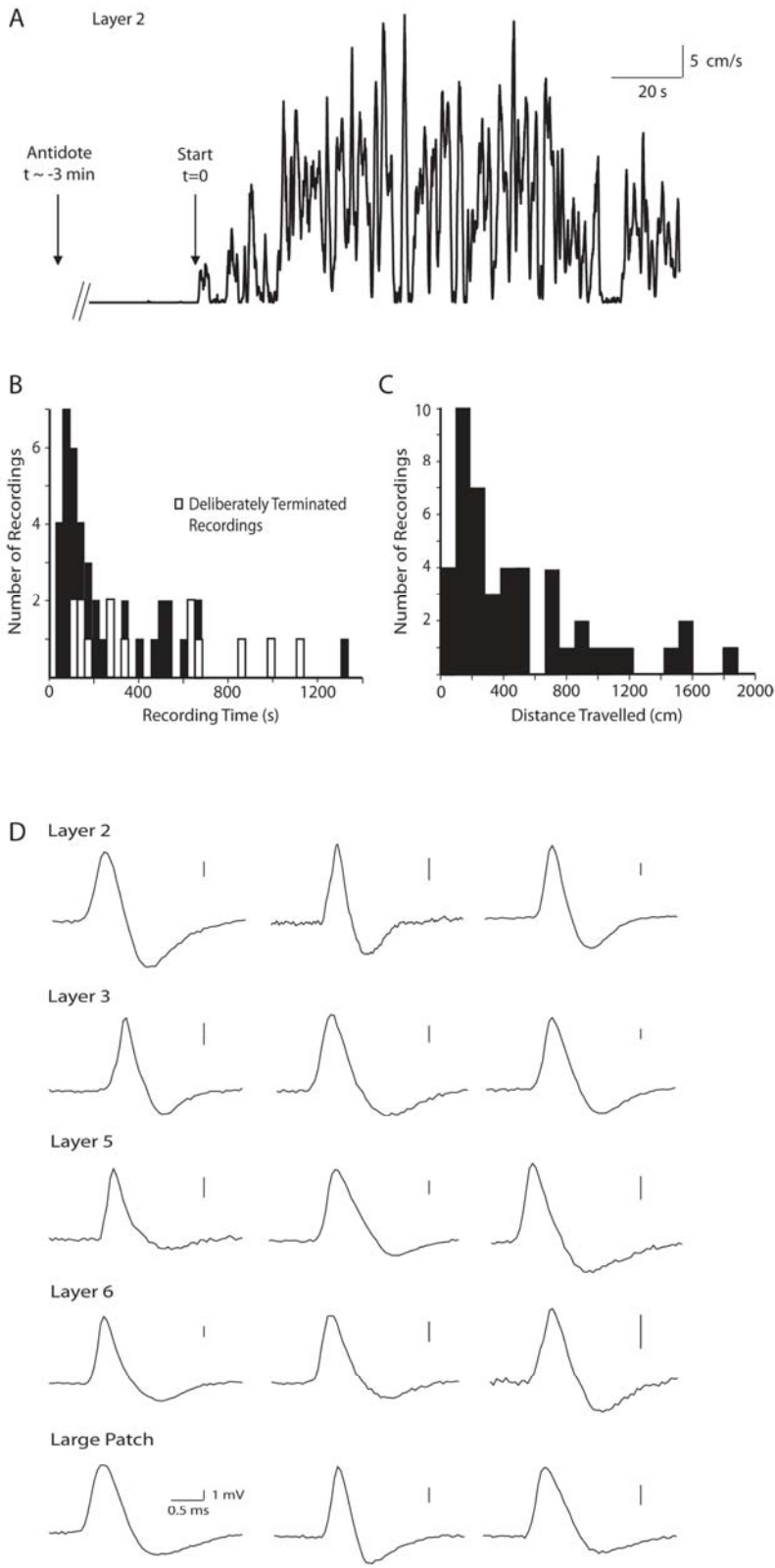
D Layer 2

Layer 3

Layer 5

Layer 6

Large Patch

1 mV

0.5 ms

Figure S1

Figure S1. Recording durations, wake-up from anesthesia and representative spike waveforms

(A) Representative speed-plot as a function of time for the recording shown in Figure 3A-E. Movement onset after wake-up (black arrow; t=0, start recording) typically occurred 2-3 minutes after injection of the antagonist.

(B-C) Distribution of recording durations (B) and total distances travelled (C) for all freely-moving juxtacellular recordings (n=46). Note that a fraction of recordings (~30%) were arbitrarily terminated to improve the rate and quality of cell recovery. These cases included: (i) recordings of silent cells; (ii) recordings where "good" spatial coverage was obtained (e.g. multiple laps run), and (iii) recordings where the peak-to-peak spike amplitude decreased to ~1 mV but was still clearly discernible. For this reason the distribution of recording durations presented provides an underestimate of the recording lengths that can be obtained with our method.

(D) Representative spike waveforms for cells recorded from layer 2, layer 3, layer 5, layer 6 and large patches, high-pass filtered at 100 Hz. Three examples from three different cells are shown for each group. Time scale (lowest left) is the same for all traces, y-scale is always 1 mV.

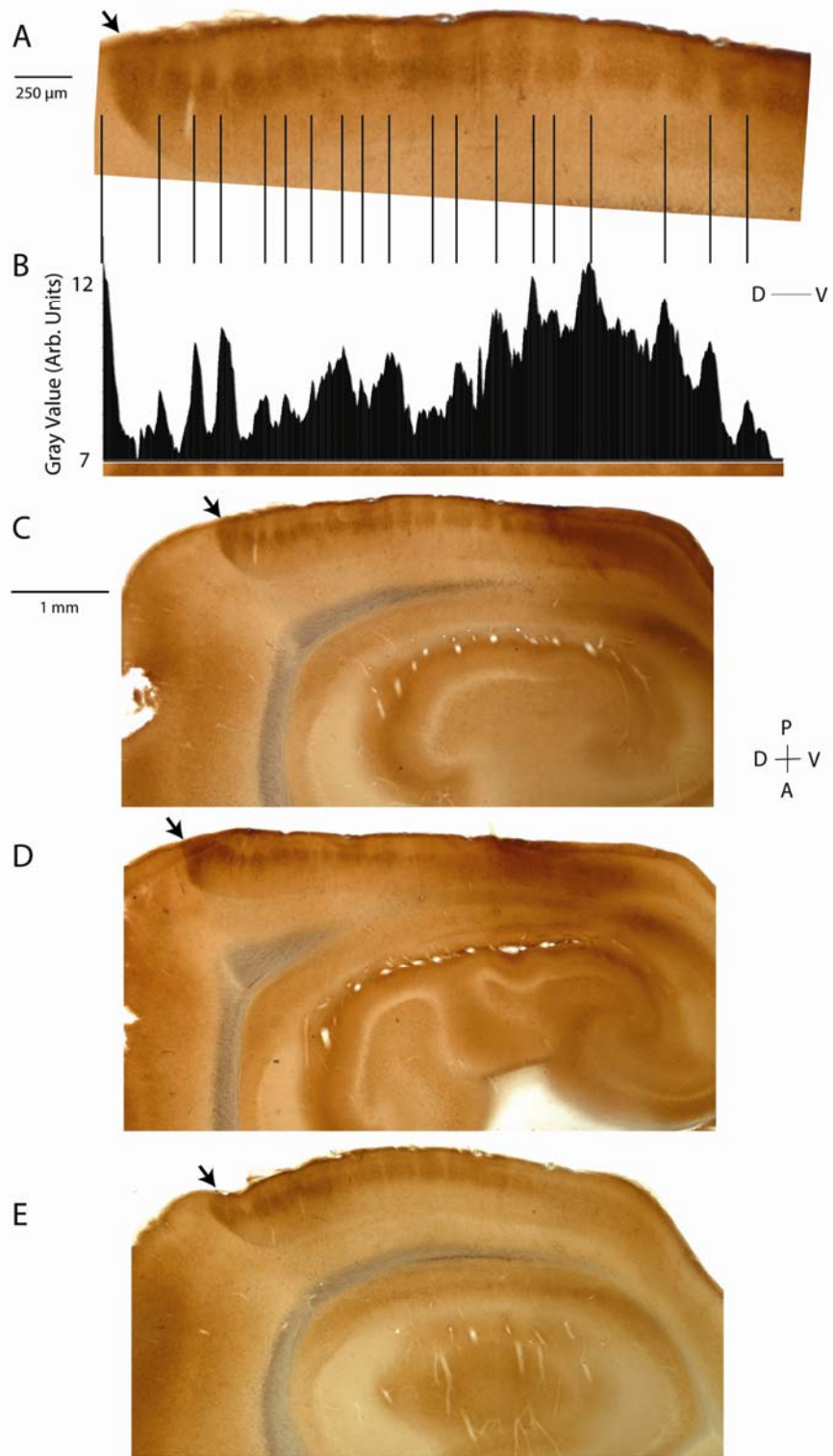This Figure is related to Figure 1 in the main text.

A

250 μm

B

Gray Value (Arb. Units)

12

7

D —— V

C

1 mm

P
D + V
A

D

E

Figure S2

Figure S2. Cytochrome oxidase staining reveals layer 2 patches in parasaggital sections of medial entorhinal cortex

(A) High magnification micrograph of a cytochrome oxidase stained parasagittal section through the center of medial entorhinal cortex; the large patch is indicated by the arrow.

(B) Bottom, longitudinal region of interest through layer 2. Top, quantification of cytochrome oxidase activity by gray scale value. The densitometric profile reveals periodic patch borders (light regions). Vertical lines indicate the alignment of patch borders to the section shown in A, from which the region of interest was taken.

(C) Low magnification micrograph of the cytochrome oxidase stained parasagittal section shown in A; the large patch is indicated by the arrow.

(D-E) 0.5 mm more medial (D) and 0.5 mm lateral (E) sections, relative to (A-C); the large patch is indicated by the arrow. Large patches extend around the full mediolateral ($\geq$ 1.5 mm) extent of medial entorhinal cortex.

D = dorsal; V = ventral, P = posterior, A = anterior. This Figure is related to Figure 2 in the main text.

A (dorsal) 0%   25%   50%   75%   100% (ventral)

B

RS ctx

L6-WM-Border   Pia

D ——— V
500 µm

Figure S3

Figure S3. Small layer 2 cytochrome oxidase patches increase in size from dorsal to ventral medial entorhinal cortex

(A) The size of cytochrome oxidase patches was quantified in different brains along a dorsoventral axis, beginning dorsally at the border of the large patch and ending at the ventral end of medial entorhinal cortex, where the cortex curves towards anterior.

(B) Drawing of small layer 2 patches (light brown) and the large patch / pair of patches (dark brown) from parasagittal sections through the mediolateral center of medial entorhinal cortex. Sections (100 μm thickness) stem from five different brains; sections of 30-100 μm thickness led to similar drawings, sections thicker than 100 μm often left the small dorsal patches difficult to discern. In some cases patches could not be unambiguously identified in the ventral parts of medial entorhinal cortex and were not drawn or quantified. Note that sectioning cuts randomly through patches; as a consequence, the drawn / quantified outlines do not necessarily reflect the full extent of each patch and patches might appear more irregular than they are *in situ*. The cytochrome oxidase stain corresponding to the top section is also shown in Figure 2. The sections drawn here were used as reference for the quantifications shown in Figure 2F. D = dorsal, V = ventral, WM = white matter. This Figure is related to Figure 2 in the main text.
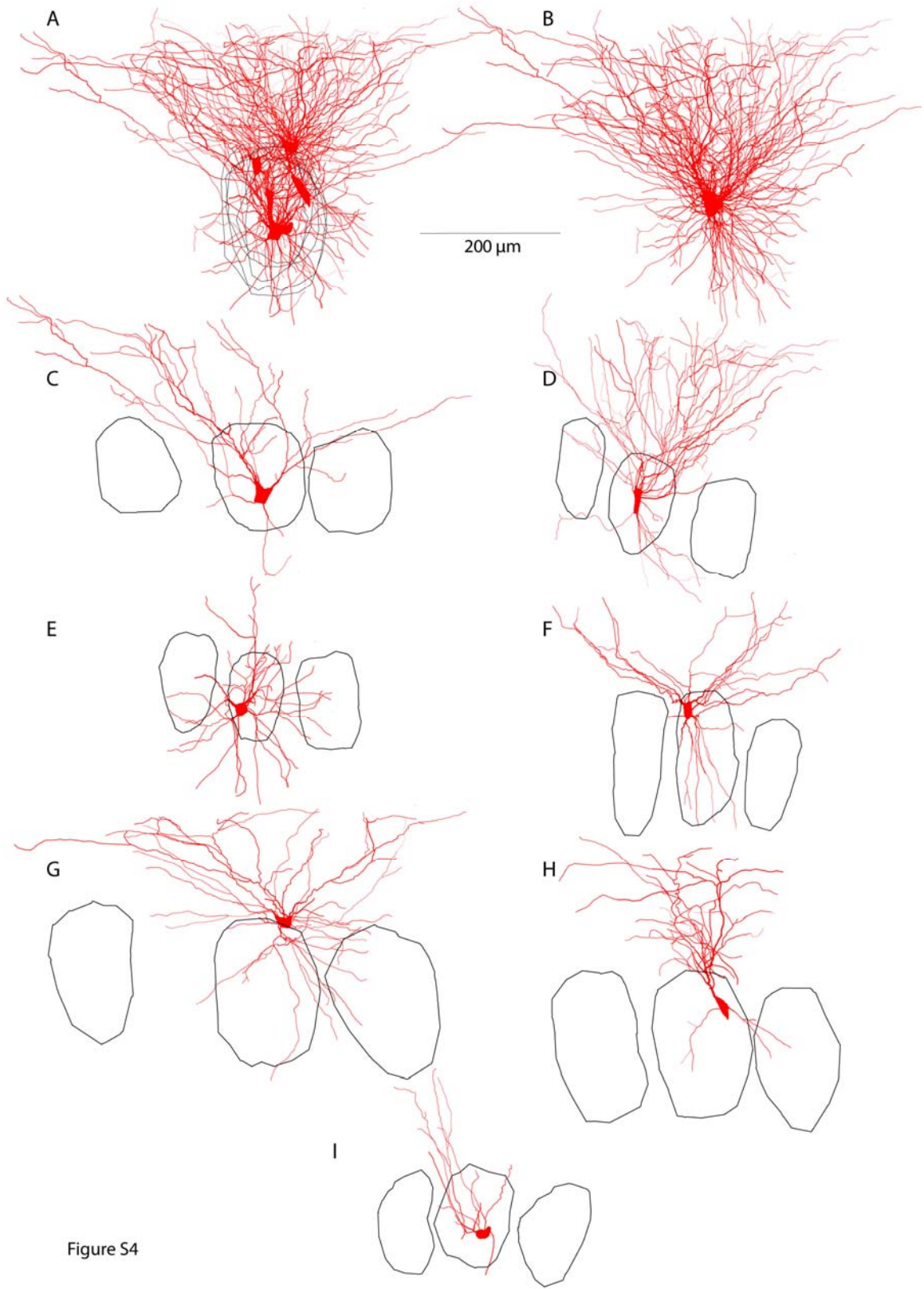
A

B

200 μm

C

D

E

F

G

H

I

Figure S4

Figure S4. Dendritic morphologies of layer 2 stellate neurons relative to the patchy layer architecture

Reconstructions of the dendritic morphologies (red) from seven layer 2 neurons, shown superimposed on outlines (black) of layer 2 cortical patches. In most cases patches were identified from cytochrome oxidase stains; in some cases high biocytin background made this impossible and we estimated patch borders from somata densities, which could always be visualized.

(A) Patch-centered superimposed dendritic reconstructions. The centers of home-patches were aligned for the superposition (black lines). Vertical orientation of cells to the *pia* was maintained for all cells. Note the wider extension of the dendritic trees in layer 1 above the patches.

(B) Same cells as in A, shown centered on the soma.

(C-I) Reconstructions of the individual neurons shown in A and B. The cell in D is the same as in Figure 3A. Note that the cell shown in E, which had the most pyramidal-like and the least stellate-like morphology, showed the least constraint by patch borders.

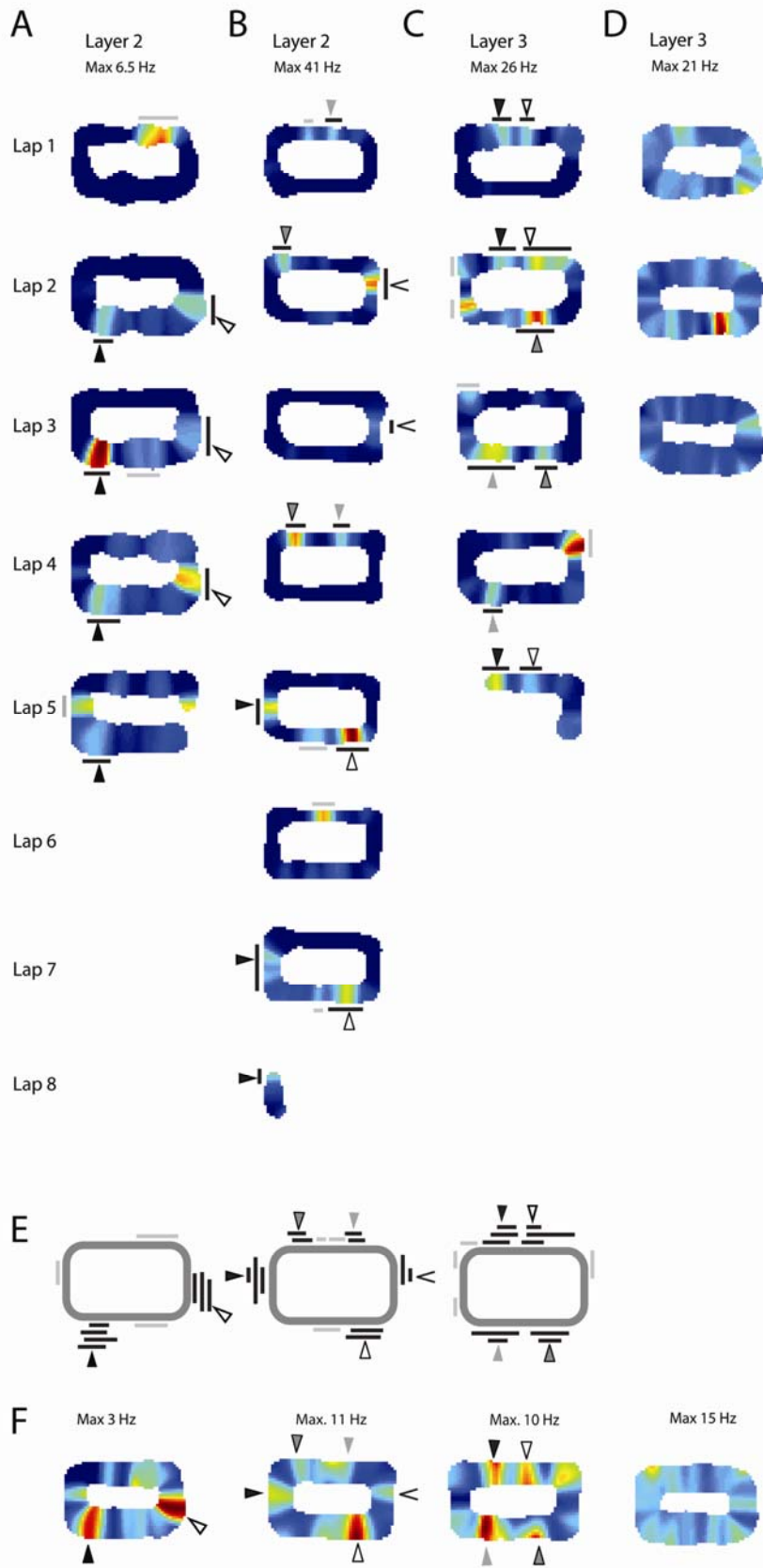This Figure is related to Figure 2 in the main text.

Figure S5

Figure S5. Lap-by-lap spatial firing analysis of superficial layer neurons

(A-D) Color-coded rate maps of individual consecutive laps for representative layer 2/3 neurons. In the neurons shown in A-C, the majority of firing fields seen in individual laps appeared in multiple laps (see arrowheads and black bars). In the layer 2 neuron shown in A, 70% of the total firing fields (7 out of 10) appeared multiple times across consecutive laps, and accounted for only 15% of the total area (see Supplemental Experimental Procedures). In the examples shown in B and C, 73% (11 out of 15) and 71% (10 out of 14) of the total firing fields occurred multiple times, and accounted for 29% and 28% of the total area, respectively. The neuron in D shows a spatially distributed firing pattern. Arrowheads of the same color indicate the same firing locations. Grey and black bars highlight firing fields which appeared once or more than once, respectively. The cell in B is the same as in Figure 3A-E, and the cell in C is the same as in Figure 3F-J. 120 x 60 cm "O"-shaped maze. Bins of 2.5 x 2.5 cm, maximum firing rate indicated above.

(E) Schematic binary representation from the data in A-C showing firing fields which occurred only once (grey) or multiple times (black) across consecutive laps. Arrowheads same as in A-C.

(F) Average color-coded rate maps for the individual laps shown in A-D. Multiple spatially-separated firing peaks are evident in the average rate maps for A-C (see arrowheads) but not for D. Arrowheads same as in A-D.

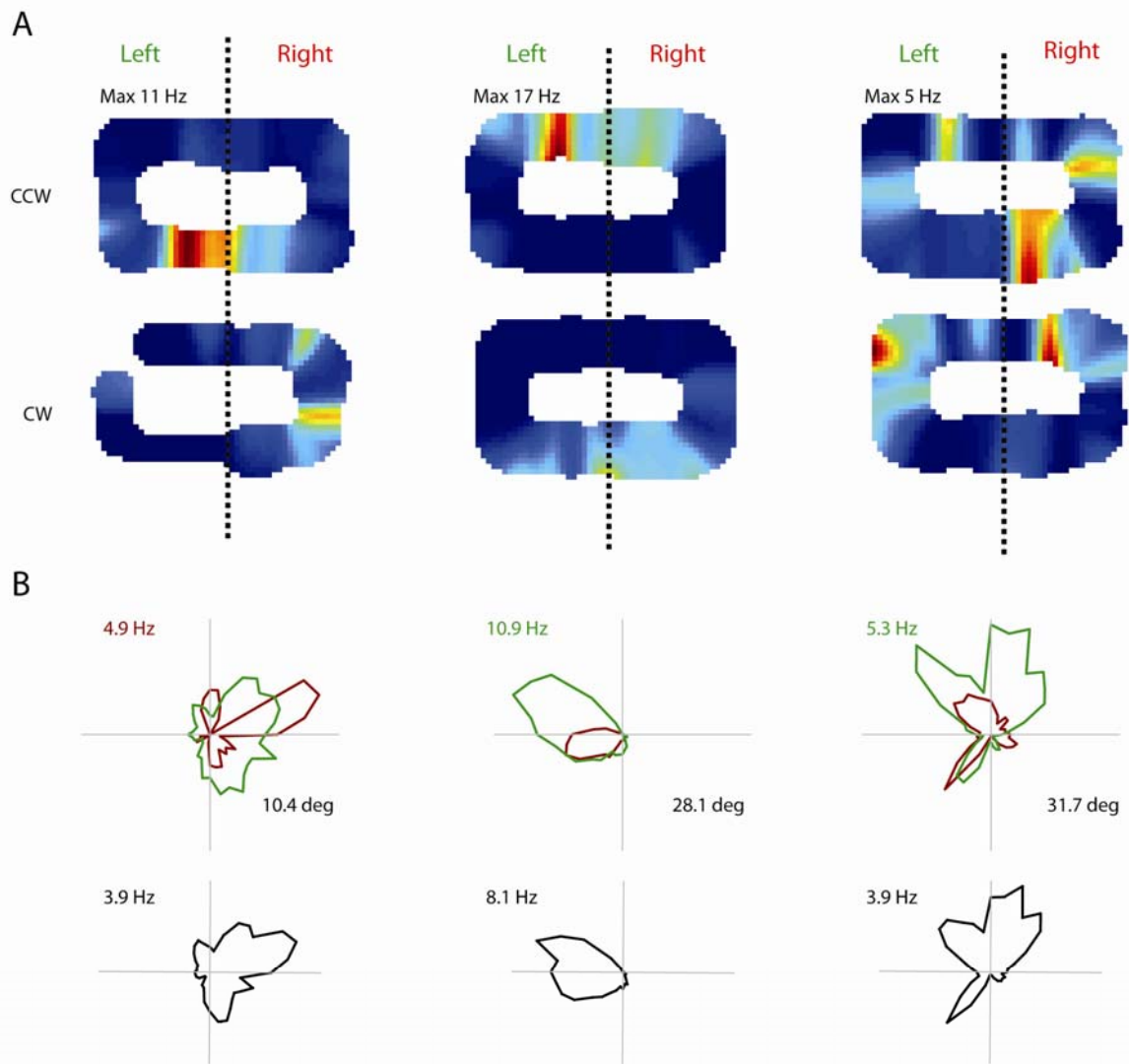This Figure is related to Figure 3 in the main text.

A

Left | Right   Left | Right   Left | Right

Max 11 Hz   Max 17 Hz   Max 5 Hz

CCW

CW

B

4.9 Hz   10.9 Hz   5.3 Hz

10.4 deg   28.1 deg   31.7 deg

3.9 Hz   8.1 Hz   3.9 Hz

Figure S6

Figure S6. Stability of head-direction firing in large patch cells

To test for the stability of head-direction selectivity and its independence over spatial locations in large patch cells, we divided the recording environment in two vertically split sub-environments, and computed head-direction selectivity separately for each one of the two sub-environments. This analysis was performed for the three large patch cells where we obtained sufficient sampling from both clockwise (CW) and counterclockwise (CCW) running directions.

(A) Color-coded rate maps shown separately for CW and CCW running directions for three large-patch cells (vertical rows). The cells in the second and third rows are the same as the ones in Figure 6G-L and Figure 6A-F, respectively. The subdivision of the recording environment in two halves (green, left; red, right) is schematically shown by the vertical dotted lines.

(B) Top, firing as a function of head-direction computed separately for the left (green) and right (red) parts of the recording environment. Note the similar head-direction tuning between the two split environments, as shown by the angular difference between the two average vectors (lower-right corner). Bottom, firing as a function of head-direction, computed for the entire recording session. Peak firing rates are indicated (top-left corner of each panel).

This Figure is related to Figures 5, 6 and 7 in the main text.

A   Layer 2   Layer 3   Large Patches

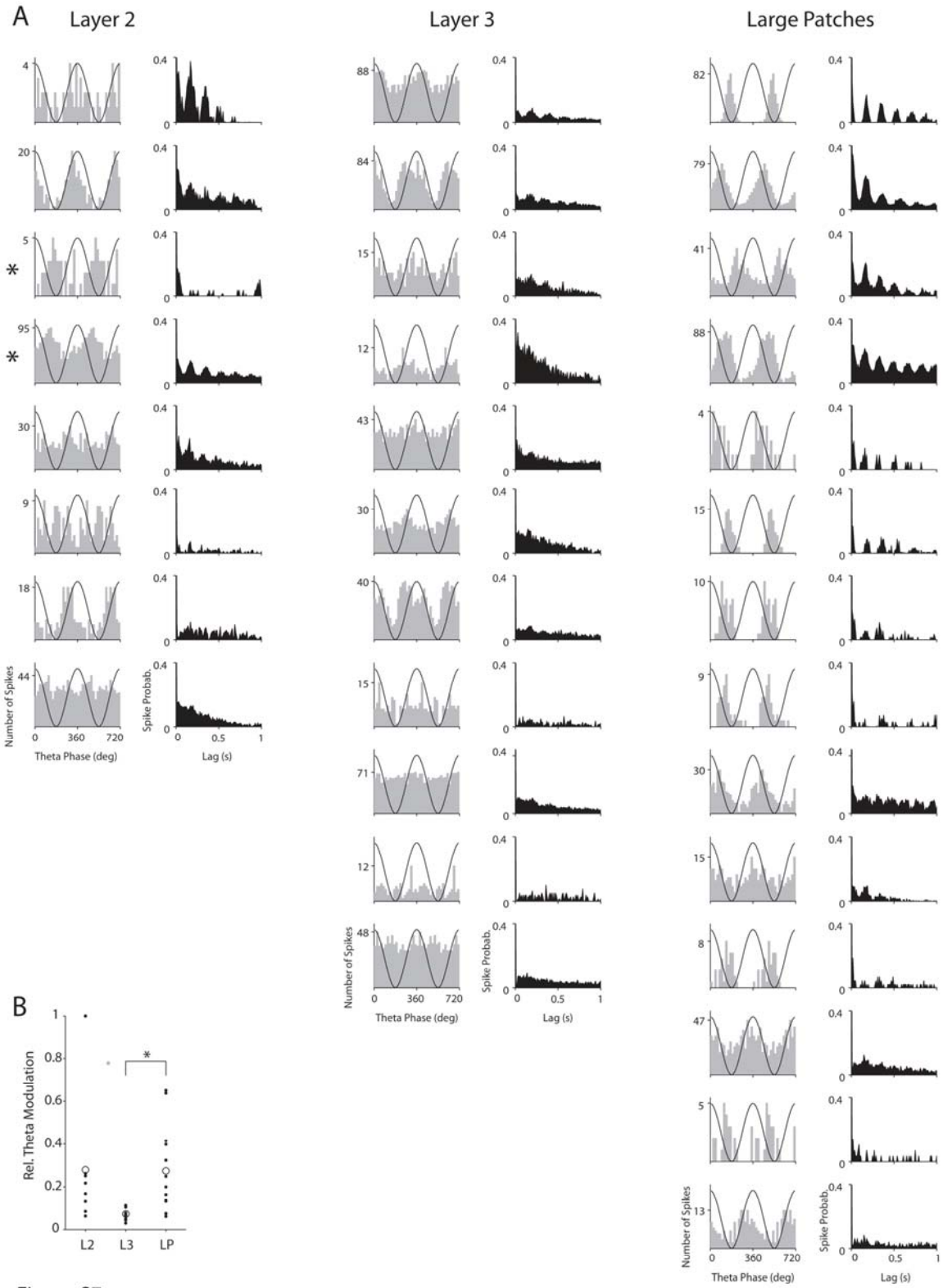Number of Spikes / Theta Phase (deg)   Spike Probab. / Lag (s)

Figure S7

Figure S7. Theta modulation and theta phase preferences of layer 2, layer 3 and large patch cells of medial entorhinal cortex

(A) Spike distributions within the theta cycle for layer 2 (n=8, left), layer 3 (n=11, middle) and large patch cells (n=14, right). Bins of 18°, two theta cycles are shown, peak of the local theta oscillation is 0°. The phase of the theta oscillation is shown in black. The asterisk (*) labels two recordings, in which the putative recording site (tip of recording pipette) was located in layer 1. For these two cells, the polarity of the locally recorded theta signal might have been inverted relative to deeper recording locations. In the right column, the corresponding autocorrelation diagrams showing spiking probability distribution for the same cell are shown.

(B) Theta modulation for cells in layer 2 (L2, n=8), layer 3 (L3, n=11) and large patches (LP, n=14). The theta modulation index was determined as the maximum of the autocorrelation function's power spectrum between 4 and 10 Hz and then normalized by the greatest value found across all cells. The grey data point refers to a cell located at the layer 2/3 border (see Results), which was not included in the analysis. The asterisk indicates significance at the 0.05 level.

This Figure is related to Figure 7 in the main text.

Depth: -20 μm

Depth: -60 μm

Putative Centrifugal
& Centripetal Axons

500 μm

D
M ┼ L
V

3

4

Depth: -100 μm

2

3

4

Depth: -140 μm

2

3

4

Depth: -180 μm

2   1

3

4

5

6

Depth: -220 μm

2   1

Putative
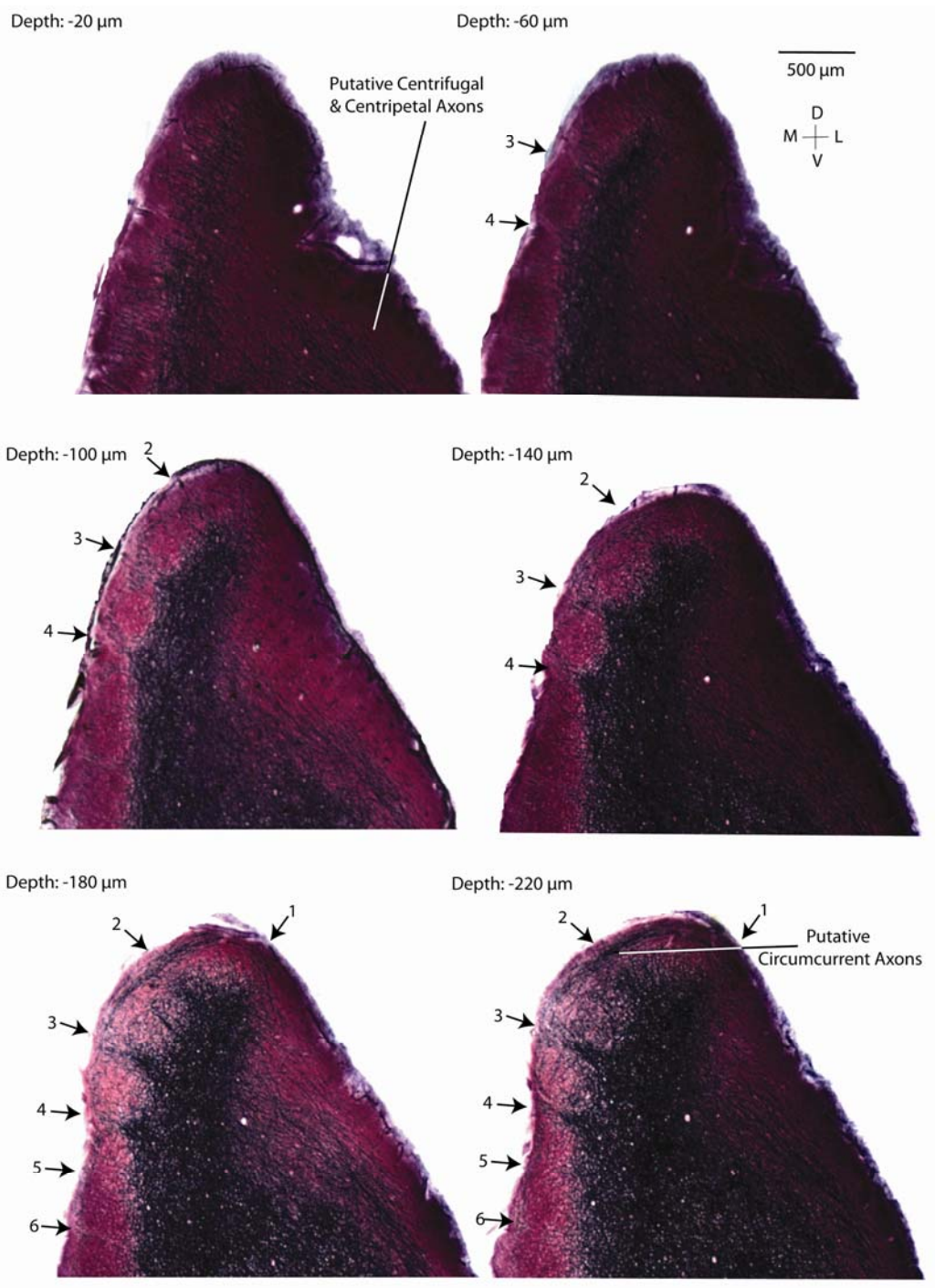Circumcurrent Axons

3

4

5

6

Figure S8

Figure S8. Myelin stained tangential sections through the dorsomedial region of medial entorhinal cortex

Myelin-stained serial tangential sections through the dorso-medial region of a right hemisphere of medial entorhinal cortex. Myelin appears black, somata whitish, neuropil violet. Medial and dorsal large patches are covered with myelin (top two sections), but the inside of the patches (bottom four sections) is largely free of myelin. Thus black septa are clearly discernible, which separate large patches and outline the patch borders. Black septa are marked with arrows and numbered consistently through all sections. Only the dorso-medial part of medial entorhinal cortex is shown, in which we identified the seven large patches shown here; about 18 additional large patches beyond the sections shown here were identified in this brain: dorsally three patches extended laterally and about 15 ventrally to the illustrated area (not shown). Note the continuity of medial patches (classically referred to as parasubiculum) and dorsal large patches. Depths refer to depth from pia at the dorsal part of each section. D = dorsal, V = ventral, M = medial, L = lateral.

This Figure is related to Figure 8 in the main text.

SUPPLEMENTAL EXPERIMENTAL PROCEDURES

Juxtacellular recording and labeling of single neurons in freely-moving animals.

Standard surgical preparation, pipette anchoring and anesthesia/wake-up procedures were performed as described previously (Lee et al., 2009). Briefly, juxtacellular recordings were obtained in experimentally naïve ~ P30-P50 male Wistar rats (130-230 g) which were maintained on a 12-h light / 12-h dark schedule and tested in the dark phase. Animals were anesthetized with an intraperitoneal dose (i.p.) of a mixture of medetomidine (225 μg/kg), midazolam (6 mg/kg) and fentanyl (7.5 μg/kg), then head-fixed into a standard stereotaxic surgical apparatus. The labeling technique was also tested in acute experiments, in which animals were anesthetized with urethane (1.5–2.0 g/kg i.p.). For targeting of the medial entorhinal cortex (left hemisphere), a small craniotomy (~2-4 mm diameter) was made 0.2-0.8 mm anterior to the transverse sinus and 4.5-5 mm lateral to the midline (Fyhn et al., 2007; Derdikman et al., 2009). A plastic ring was glued around the craniotomy and filled with Ringer solution.

The friction-based pipette drive (L.H. et al., manuscript in preparation) was anchored to the skull by application of dental acrylic after positioning the pipette tip at the center of the craniotomy with a stereotaxic apparatus. A metal post for head-fixation and placement of the pre-amplifier (ELC Ultra miniature headstage, Npi Electronics, Tamm, Germany) was also cemented to the skull posterior to the microdrive´s guide (Figure 1).

Blind *in vivo* juxtacellular recordings were obtained using previously described procedures (Houweling et al., 2010) at targeting depths of ~1700-3200 μm from the pial surface. Pipettes (4-6 MΩ) were filled with extracellular (Ringer) solution containing (in mM) NaCl 135 (Roth Gmbh, Karlsruhe, Germany), KCl 5.4, HEPES 5, $CaCl_2$ 1.8 (Roth Gmbh), and $MgCl_2$ 1 (pH 7.2) as well as biocytin (2-3%). All chemicals, unless otherwise stated, were from Sigma-Aldrich (Taufenkirchen, Germany). After a juxtacellular recording was obtained, the cell was stained by injecting a 200 ms square-wave current pulse into a neuron through a glass pipette (Houweling et al., 2010) and current strength was adjusted (typically in the 1-10 nA range) to elicit AP firing without damaging the neuron. Depending on the intensity of firing elicited by the current injections, cells were "entrained" for typically 1-5 min. Cells which did not fire APs during the behavioral

session ("silent" cells) were always fired by current injections at the end of the recording trial to verify the presence of the neuron. Freely-moving recordings were terminated either by sudden loss of spike signals due to mechanical disturbances, or arbitrarily (e.g. after multiple laps run or reduction of peak-to-peak spikes amplitude below 1mV) to improve the rates and quality of cell recovery.

Dental acrylic was carefully applied in order to anchor the pipette rigidly with respect to the skull. After the acrylic had hardened (~10 min), the animal was removed from the stereotaxic apparatus and moved to the "O"-shaped behavioral arena (~ 60 × 120 cm, ~ 22 cm high inner and outer walls, ~ 12 cm wide path between the inner and outer walls). For a small subset of cells, a smaller "O"-maze (~ 40 × 80 cm, n=8) and rectangular arenas (~ 190 × 190 cm and ~ 60 × 40 cm, n=5) were used. Once the animal had been placed in the arena, the anesthetic mix was than antagonized with a subcutaneous dose of a mixture of antipamezole (1 mg/kg), flumazenil (600 μg/kg) and naloxone (180 μg/kg).

The juxtacellular signal was amplified by an ELC-03XS amplifier (NPI Electronic) and sampled at 20 kHz by a LIH 1600 data-acquisition interface (HEKA Electronic, Lambrecht/Pfalz, Germany) under the control of PatchMaster 2.20 software (HEKA Electronic). The weight of the implant and the pre-amplifier on the rat´s head was balanced by counterweight cables in order to allow the animal to move freely in space. The animal's behavior in the maze was videotaped and its location and head-direction automatically tracked at 25 Hz by the Digital Lynx videotracking system (Neuralynx, Boseman MT, USA). For video tracking, two LEDs (red and blue) separated by 4.5 cm, were placed on the animal´s head. At the end of recording, the animal was injected with an overdose of ketamine or urethane and quickly perfused transcardially with 0.1 M phosphate-buffered saline followed by a 4% paraformaldehyde solution.

For targeting of "large" patches at the dorsal border of medial entorhinal cortex, animals were implanted under ketamine/xylazine anesthesia (100 and 5 mg/kg, i.p., respectively) with a metal post for head-fixation and a recording chamber, as described previously (Houweling et al., 2008). Craniotomies were performed 0.2 mm anterior to the sinus and 4.5-5 mm lateral to the midline. After 2-3 days of habituation to head-fixation, awake rats were head-fixed by the metal post and extracellular recordings were performed with either conventional glass-pipettes (2-4 MΩ) or tungsten electrodes (Resistance = 0.5

MΩ). The target depth was estimated by lowering the recording glass-pipette filled with extracellular solution or the tungsten electrode, while listening to the extracellular activity using an audio monitor. The depth at which a sudden increase in theta modulation of field activity and/or recorded spikes was observed, was noted as the recording depth for subsequent juxtacellular recordings. Head-fixed animals were then anesthetized, and the experiment was performed as described above. In a subset of experiments, the large patches at the dorsal border of medial entorhinal cortex were targeted without previous extracellular mapping in awake animals, by monitoring the change in the LFP pattern (not shown) observed under anesthesia at the transition from retrosplenial cortex. All experimental procedures were performed according to German guidelines on animal welfare.

Histology

Rats were killed by an overdose of urethane or ketamine, and perfused transcardially with 0.9% phosphate buffer saline solution, followed by 4% paraformaldehyde in 0.1 M phosphate buffer. Brains were removed from the skull and immersed in fixative for at least one day. To reveal the cell morphology of juxtacellularly-labeled cells, brains were sectioned in 100-150 μm thick parasagittal slices, which were then processed with the avidin-biotin-peroxidase method essentially as described previously (Lee et al., 2006; Lee et al., 2009; Epsztein et al., 2010), with the exception that we typically used longer incubation times (up to 1 hour) in the peroxidase-substrate solution to maximize staining intensities. Sections were then mounted with Moviol on glass coverslips. In most slices, additional cytochrome oxidase staining was performed (see below) to visualize the patchy organization of medial entorhinal cortex. Neurons were reconstructed with Neurolucida software (MBF Bioscience, Williston VT, USA) and displayed as two-dimensional projections. In several cases, background from the biocytin stain made it difficult to recognize cytochrome oxidase patches directly adjacent to the neuron. In these cases we outlined the small layer 2 patches adjacent the neuron by the increased density of somata, which was always visible. In all neurons included (n = 46) dendrites were recovered. In ten cases, however, the full dendritic tree was not preserved and in these cases dendritic morphology was not classified. Stained cells were identified based on

labeling intensity and the presence of an electrode track, which – perhaps as a result of the mechanical strain during the animal's movements – was always clearly identifiable. Specifically we observed in a majority of cases staining of a single strongly labeled cell with dendrites that were labeled as strongly or even more strongly than the soma, in addition to weakly labeled cells, in which the somatic labeling was stronger than dendritic labeling. In all of these cases the electrode track targeted the strongly stained neuron and all of these cases were included. In other cases the staining differences between cells were quantitative rather than qualitative. In these cases we included the neuron if the electrode track targeted the cell with the most strongly stained dendrites. All other cases were excluded.

For histochemical analysis, brains were immersed in 30% sucrose solution for cryoprotection and subsequently embedded in a mixture of egg yolk, 30% sucrose supplemented by 0.75 mL glutaraldehyde. 40 μm-thick sections were obtained with a cryostat (Leica 2035 Biocut). Four plans of section were used: coronal, horizontal, tangential (= parallel to the pial surface of medial entorhinal cortex, at a sectioning angle of ~45° to the horizontal plane) and parasagittal. Alternating sections were processed for Nissl, cytochrome oxidase, and myelin stainings. Cytochrome oxidase and Nissl staining were essentially performed as described previously (Wong-Riley 1979; Brecht and Sakmann, 2002). Densitometric analysis of cytochrome oxidase activity in Figure S2 was performed with the ImageJ Software (NIH). For quantification of patch sizes, the minimum and maximum Feret diameter (defined as the shortest and longest dimension of the patch, respectively) were determined using Neurolucida software (MBF Bioscience) for each patch, and averaged across 25% bins of the dorso-ventral axis. Five sagittal sections through the center of medial entorhinal cortex (from five animals) were used for the analysis. For myelin stainings, a variation of the gold-chloride protocol (Schmued 1990) was used. Briefly, free-floating cryostat sections were incubated for 2-4 hours in a 0.1% solution of gold chloride in a solution containing 0.02 M phosphate buffer and 0.9% NaCl (pH 7.4). After staining, sections were rinsed and fixed for 5 min in a 2.5% solution of sodium thiosulfate before being mounted on glass coverslips. In myelin stained tangential sections (40 μm thickness), large patches at the dorsalmost border of medial entorhinal cortex were detected by massive axons bundles on the dorsal surface of

each patch (as in Figure S7), while small layer 2 patches were detected in mid-depth of layer 2 as clusters of white somata surrounded by myelin.

Data analysis

Spike analysis

During the freely-moving recording session (i.g first animal movement after waking-up from anesthesia) the peak-to-peak spike amplitude was on average 4.6 ± 2.2 mV, corresponding to 41.2 ± 22.7 times the root mean square amplitude of the noise. Spikes amplitude was generally stable (± 30-40% of the initial value) during the freely-moving recording sessions, while in some trials it slowly decreased over time. A three-dimensional analysis using time and the first two principal components of the wave form was performed to visualize and assess the stability of spikes amplitude over time, and to isolate spikes from recording artifacts. The duration of the trial was defined as the time at which the rat moved after waking-up from the anesthesia to the time of the last included spike. Data are expressed as mean ± standard deviations.

Analysis of Spiking Modulation

The position of the rat was defined as the midpoint between the two head-mounted LEDs. The behavior of the animal was classified as exploratory or awake but resting ("rest"), according to the running speed analysis (cut-off of 0.2 cm/s applied to the speed averaged across a 600 ms rectangular sliding window). To illustrate the modulation of firing rate with head location, color-coded firing maps were plotted. For these, space was discretized into pixels of 2.5 cm x 2.5 cm, for which the occupancy z of a given pixel x was calculated as

$$z(x) = \sum_t w(|x - x_t|)\Delta t$$

where x_t is the position of the rat at time t, Δt the inter-frame interval, and w a Gaussian smoothing kernel with $\sigma = 5$ cm (Harris et al., 2001).

Then, the firing rate r was calculated as

$$r(x) = \frac{\sum_i w(|x - x_i|)}{z}$$

where x_i is the position of the rat when spike i was fired. The firing rate of pixels whose occupancy z was less than 20 ms was considered unreliable and not shown.

Head-direction tuning was measured as the excentricity of the circular distribution of firing rates. For this, firing rate was binned as a function of head-direction (n=36) and Rayleigh's average vector calculated. The head-direction index of a cell was then defined as this vector length divided by its average firing rate across the circular distribution. For spatial and head-directional analysis, both a spatial (> 2 laps covered) and a firing rate inclusion criterion (> 0.5 Hz) were applied. Recordings from 26 out of 40 non-silent cells passed these criteria and were included in the analysis. From deep layers, only one layer 6 neuron satisfied the inclusion criteria, but was not included in the analysis.

To assess spatial modulation, cells were ranked according to the extent to which firing repeated in restricted spatial locations. This factor takes into account the fraction of firing fields appearing multiple times across consecutive laps and the fraction of the total area they cover (% Repeating Firing Fields / % Area Repeating Firing Fields). For a large fraction of layer 2/3 recordings (6 out of 13) the ratio was between 2 and 4 (Figure S5B and S5C and not shown); for two layer 2 cells the ratio was > 5, indicating a strong preference for firing to occur in spatially restricted areas (Figure S5A and not shown).

Clockwise and counter-clockwise running directions were defined by the angle between the rat's head direction and the hypothetical line connecting the rat's head to the center of the maze. Angles between 0 and 180° were counted as clockwise, and otherwise counter-clockwise.

A neuron's theta modulation was determined by first calculating the spike train's autocorrelation function, binned at 10 ms. To measure modulation strength in the theta band, the maximum of the autocorrelation function's power spectrum between 4 and 10 Hz was determined. Statistical significance of between-layer differences was assessed by a Kruskal-Wallis global test with Tukey-style post-hoc pairwise tests (data in Figure 7A and Figure S7B), or a Wilcoxon rank-sum test (data in Figure 7B).

For spike-theta phase analysis, juxtacellular signals were band-pass filtered at 4-10 Hz, and a Hilbert transform was used to determine the instantaneous theta phase of the filtered theta wave (peaks = 0, 360° and troughs = 180°). Then, each spike was assigned

the theta phase of the Hilbert transform at the time of that spike. Only spikes during walking/running (speed threshold = 0.2 cm/s) were included in the analysis.

To estimate the modulation strength of each layer, the Rayleigh average vector of spikes' theta phases was calculated for each cell and then averaged across each neuronal sub-population (i.e. layer 2, layer 3 and large patches). Statistical significance of each subpopulation's modulation strength was assessed with a permutation test that ranked the length of each subpopulation's average vector in a distribution of 1000 shuffled average vectors, computed by assigning random phases to all cells of that subpopulation while maintaining their lengths.

The between-populations phase differences were calculated as the angular difference between two populations' Rayleigh vectors. Its significance was computed by ranking the phase difference in a distribution of 1000 shuffled differences obtained by permuting the cells' affiliations.

Spike distributions within the theta cycle were computed for each cell by using bins of 18°. Averages across subpopulations as in Figure 7G were computed by normalizing each cell's theta distribution histogram by the total number of spikes and then taking the binwise mean across all cells of a subpopulation. A rectangular smoothing of 5 bins (corresponding to 90°) was applied.

SUPPLEMENTAL EXPERIMENTAL REFERENCES

Harris K.D., Hirase, H., Leinekugel, X., Henze, D.A., Buzsáki, G. (2001) Temporal interaction between single spikes and complex spike bursts in hippocampal pyramidal cells. Neuron *32*, 141–149

Houweling, A.R., Doron, G., Voigt, B.C., Herfst, L.J., Brecht, M. (2010) Nanostimulation: manipulation of single neuron activity by juxtacellular current injection. J. Neurophysiol. 103, 1696-704

Houweling, A.R. and Brecht, M. (2008) Behavioural report of single neuron stimulation in somatosensory cortex. Nature *451*, 65-8